Nuclear Science and Techniques (2024) 35:130
https://doi.org/10.1007/s41365-024-01484-4

Spatial- and spin-resolution ARPES and magnetism beamline at SSRF

Fang-Yuan Zhu[1] · **Jie-Feng Cao**[1] · **Xiang-Yu Meng**[1] · **Jun-Qin Li**[1] · **Rui Yu**[1] · **Ya-Mei Wang**[1] · **Shan Qiao**[2] · **Bo Zhao**[1] · **Ming-Zhu Zhang**[3] · **Zhong-Kai Liu**[2] · **Mei-Xiao Wang**[2] · **Yong Wang**[1] · **Ren-Zhong Tai**[1]

Received: 22 September 2023 / Revised: 26 December 2023 / Accepted: 28 December 2023 / Published online: 21 July 2024

Abstract

The BL07U beamline is a new extreme ultraviolet and soft X-ray beamline housed in the Shanghai Synchrotron Radiation Facility. Beamlines are used in nano-resolved angle-resolved photoemission spectroscopy (nano-ARPES), spin-resolved angle-resolved photoemission spectroscopy (spin-ARPES), X-ray magnetic circular dichroism spectroscopy, and X-ray magnetic linear dichroism spectroscopy for certain scientific research. The BL07U beamline, which is based on a pair of elliptical polarized undulators and a variable-included-angle plane-grating monochromator, delivers circularly or linear polarized X-rays within the energy range of 50–2000 eV. The beamline features two branches: One dedicated to nano-ARPES, which has a minimum spot size of only ~ 200 nm, and another branch comprising spin-ARPES, a vector magnetic field, and superconductive magnetic end-station.

Keywords Soft X-ray beamline · Nano-ARPES · Spin-ARPES · XMCD/XMLD

1 Introduction

Angle-resolved photoemission spectroscopy (ARPES) is widely conducted for synchrotron radiation devices [1–5]. In recent years, ARPES has been further developed into nano-resolved ARPES (nano-ARPES) and spin-resolved ARPES (spin-ARPES), which have been utilized successfully for scientific endeavors and technological development [6–10]. Nano-ARPES can focus X-rays down to the submicron scale, thus enabling investigations into low-dimensional materials and nanodomain structures. Studies based on nano-ARPES have been published recently [11–13]. The superior spot size allows one to examine sum-micron-scale properties within materials, which is comparable to the conventional ARPES [14]. Spin-ARPES can separate electrons with different spins to obtain the dispersion of spin-splitting bands. Qiao *et al.* were the first to develop a spin-polarimeter system with an imaging-type exchange scattering function, which maximizes the efficiency of spin measurement using ARPES [15]. The two ARPES end-stations involved alleviate the deficiency of certain measurements at the Shanghai Synchrotron Radiation Facility (SSRF) and promote research in Mainland China using multiple methods. The development of ARPES technology is beneficial to the third- and fourth-generation synchronous devices because it can provide high fluxes, high-energy resolutions, and adjustable polarization X-rays. Additionally, owing to these advantages, X-ray magnetic circular dichroism/X-ray magnetic linear dichroism (XMCD/XMLD) technology is widely used in the third-generation synchrotron radiation [16]. XMCD/XMLD technology presents unique characteristics in the study of magnetism [17]; magnetic studies are being pursued continuously in China [18, 19], and in situ XMCD/XMLD facilities within synchrotron radiation are highly desired. Therefore, an XMCD experimental station was constructed on the beamline 07U. In the Shanghai Light Source Phase II project, we designed and constructed a beamline that encompassed the extreme

---

✉ Jie-Feng Cao
caojf@sari.ac.cn

Yong Wang
wangyong@sari.ac.cn

Ren-Zhong Tai
tairz@sari.ac.cn

[1] Shanghai Synchrotron Radiation Facility, Shanghai Advanced Research Institute, Chinese Academy of Sciences, Shanghai 201204, China

[2] ShanghaiTech Laboratory for Topological Physics, School of Physical Science and Technology, Shanghai Tech University, Shanghai 201210, China

[3] University of Chinese Academy of Sciences, Beijing 100049, China

ultraviolet and soft X-ray ranges, as well as constructed both nano-ARPES and spin-ARPES end-stations.

The construction of the BL07U beamline and four end-stations was completed in June 2021, and they have been opened to users since January 2022: the four end-stations are the vector magnetic, superconductive magnetic, nano-ARPES, and spin-ARPES end-stations. Herein, the new BL07U beamline at the SSRF for ARPES and XMCD is reviewed, including the beamline optical layout and the elements constituting the various optical sections. The energy-resolving power is analyzed using the absorption spectra of N_2 and Ne, four experimental end-stations are introduced, and the experimental results are summarized.

2 Beamline setup

2.1 Light source

Considering both the ARPES and XMCD/XMLD methods with certain energy ranges, the energy range for the beamline was selected to be 50–2000 eV. To encompass this wide energy range, two APPLE-II type elliptically polarizing undulators (EPUs) installed in parallel were used as insertion devices. This insertion device was developed by the SSRF, and when two EPUs are switched to one another, the electron beam cannot be cut off, which is similar to the case of the insertion device at the BL09U beamline [20, 21].

The two EPUs arranged in parallel are U90 encompassing the medium-to-low-energy range (50–800 eV) and U58 encompassing the medium-to-high-energy range (600–2000 eV). Limited by the total length of 5 m of the straight section, the length of each EPU was approximately 4.8 m; the specific parameters are listed in Table 1.

The two EPUs arranged in parallel can encompass a wide range of energies: Linear horizontally polarized light can include the entire range of 50–2000 eV, the lowest energy of the linear vertically polarized light can include 90 eV, and the circularly polarized light can include 70–1900 eV. To suppress harmonics, U90 is designed with a quasi-periodic structure, and the ratios of its third, fifth, and seventh harmonic fluxes to the fundamental wave at 50 eV are less than 8%. Owing to the limitations of the storage ring space, U58 and U90 can only emit line-polarized light in any direction in the one-third and two-fourth phase limits, respectively.

2.2 Beamline optics

The optical design of the beamline is based on a vertically dispersing variable-included-angle variable-line-spacing plane-grating monochromator (VLS-PGM), which allows the meridional thermal deformation of PM2 (see Fig. 1) to be compensated by changing the C_{ff} value (fixed focus constant). The three variable-line-spacing (VLS) gratings ensure a high flux and/or high resolving power over a wide energy range.

The optical layout of the BL07U beamline is illustrated in Fig. 1. The X-ray emitted from the EPU passes through the front end and aperture and is then radiated onto the first mirror (M1) with a grazing incidence angle of 1°. M1, which is located at 22 m, absorbs most of the heat, thus restraining high-order harmonic radiations [22]. The monochromator, which is located at 27 m, comprises a plane mirror and three gratings. The three gratings are variable groove depth and

Table 1 Specific parameters of BL07U EPUs at SSRF

Undulators	U90	U58
Period length (mm)	90	58
Magnetic length (m)	4.77	4.872
Number of periods	53	84
Minimum gap	21	16.5
Polarization modes	Circular/elliptical/linear (0–90°)	Circular/elliptical/linear (0–90°)
Max. magnetic field (horizontal polarization) (T)	$B_y = 0.839$	$B_y = 0.785$
Max. magnetic field (vertical polarization) (T)	$B_x = 0.839$	$B_x = 0.558$
Max. magnetic field (circular polarization) (T)	$B_x = B_y = 0.593$	$B_x = B_y = 0.463$
Lowest energy (horizontal polarization) (eV)	50	200
Lowest energy (vertical polarization) (eV)	90	370
Lowest energy (circular polarization) (eV)	70	275
Max. total power	7.8 kW @50 eV	7 kW @200 eV
Linear polarization direction	Linear polarization can be adjusted continuously from horizontal to vertical in any directions	
Additional	Dual EPU parallel switching	

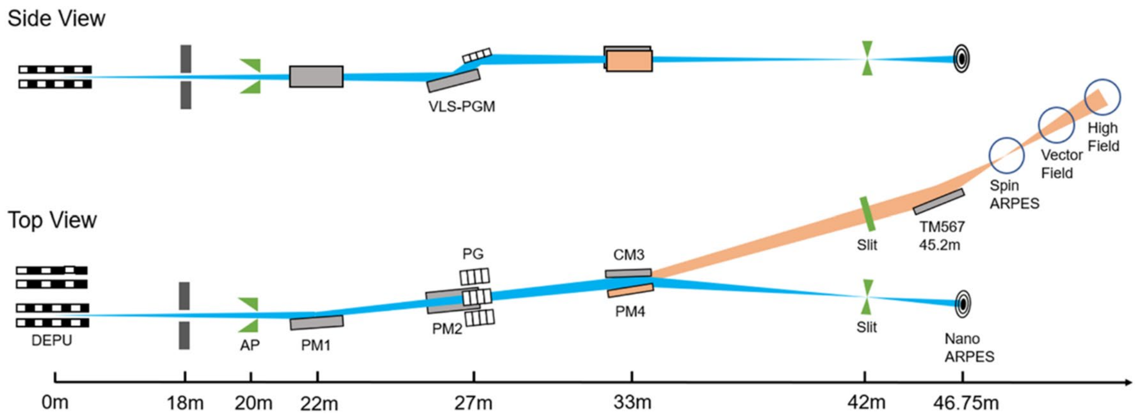

Fig. 1 (Color online) Optical layout of SSRF BL07U

VLS gratings with linear densities of 400, 800, and 1200. The VLS gratings dispersed the photon energy of the beam and vertically focused the beam onto the exit slit.

Downstream of the monochromator, a deflection mirror system comprising cylindrical mirror CM3 and plane mirror PM4, is installed to separately deflect the X-ray to two branches. One branch reaches the nano-ARPES end-station, which uses a zone plate to focus the X-rays and requires a circular light spot. Therefore, cylindrical mirror CM3 was set at 33 m to focus the beam horizontally onto the exit slit to ensure that the horizontal and vertical divergences of the beam after the exit slit were identical. In another branch, the spin-ARPES, vector field, and high-field end-stations were installed successively in the downstream direction. The focusing mirror, TM567, is a mirror with three toroids polished on a silicon substrate. The three toroids can be switched up/down to focus the beam onto the three end-stations. In this case, the spot size is minimal and suitable for small/fine or inhomogeneous samples. In other applications, two toroids were selected to obtain a large defocused spot, as in X-ray absorption spectra (XAS) measurements. Various beam spots can be switched between experimental stations for scientific research. Because of the spin-ARPES end-station, the vector field magnetic and the high-field magnetic end-stations were arranged in parallel successively to share the same X-ray beam *via* the optics switch-over, thus allowing one of the end-stations to perform the experiment at any one time, as shown in Fig. 1.

The beamline control-system software was developed using the Experimental Physics and Industrial Control System (EPICS) package. Based on the distributed features of the EPICS, three layers of hardware were implemented: an operator interface (OPI), an input/output controller, and drivers or monitors. The OPI is an operating the interface with the Linux operating system and EPICS up-level tools. The entire system operates stably and provides a flexible operating environment that satisfies user requirements.

The characteristics of all the optical elements are summarized in Table 2.

The energy-resolving powers of the three gratings are summarized in Fig. 2. The fluxes at the spin-ARPES/XMCD branch sample point and the nano-ARPES sample point, which is after the zone plate, are shown in Fig. 3.

A gas cell was permanently installed on the beamline downstream of the exit slit [23]. Monochromatic X-rays ionize gas in the cell and generate ion electron pairs. The positive ions are accelerated toward the MCP by the gold grid with negative pressure and then gathered by the MCP (MCP33ZLAF).

Figure 4 presents the N_2 $1s \rightarrow \pi^*$ absorption spectrum, which was measured using G2 (800 L/mm) with the exit slit open at 12 μm. Six absorption peaks were distinguishable from the experimental spectra; thus, six Voigt profiles were superimposed for fitting. By setting the Voigt linewidth ΔL to 113 meV [24], we obtained a Gaussian width of 26 meV ± 1 meV and a resolving power of 1.5×10^4. Another method involving the ratio between the first valley and third peak can be used to determine the energy-resolving power. The smaller the ratio, the higher is the energy resolution of the beamline. For the absorption spectrum shown in Fig. 4, the ratio is 0.66, which is almost identical to the value reported in the literature [25]. This proves that the energy-resolving power is higher than 10,000, which is consistent with the Voigt fitting result.

Figure 5 shows Ne K-edge absorption spectrum, including four fine structure resonances, *i.e.*, $1\ s \rightarrow 3p$, $4p$, $5p$, and $6p$, measured by G1 (1200 L/mm). The Ne spectra were fitted to a Lorentzian linewidth of 230 meV [26]. This yielded a Gaussian width of 66 meV ± 2 meV, which corresponded to a resolving power of 13,000.

Table 2 Optical parameters

	PM1	PM2	G1	G2	G3	CM3	PM4	TM567
Shape	Plane	Plane	Plane	Plane	Plane	Cylinder	Plane	Triple toroid
Position (m)	22		27	27	27	33	33	45.2
Geometrical surface size (mm^2)	410 × 50	520 × 50	130 × 50	130 × 50	130 × 50	380 × 50	380 × 50	500 × 100
Optical surface size (mm^2)	350 × 30	460 × 30	120 × 40	120 × 40	120 × 40	360 × 30	360 × 30	470 × 30 (3 segments)
Grazing incidence angle (°)	1	Variable	Variable	Variable	Variable	1.4	1.4	1.3
Water cooling	Side	Inside	Side	Side	Side	Side	Side	
Blank material	Single-Crystal Silicon							
Coating material	Au (> 50 nm) with Cr binder layer							
Radius of curvature (mm)						578,862		$R = 382{,}522$, $\rho = 87.119$; $R = 579{,}990$, $\rho = 102.572$; $R = 704{,}020$, $\rho = 109.181$;
Slope error (tangential/sagittal) (μrad^2)	0.2 × 2	0.2 × 2	0.2 × 2	0.2 × 2	0.2 × 2	0.7 × 5	0.7 × 5	0.7 × 5
Roughness (r.m.s) (nm)	0.3							
Line density (center) (l/mm)			400	800	1200			
Groove depth (nm)			10–30	8–18	6–16			

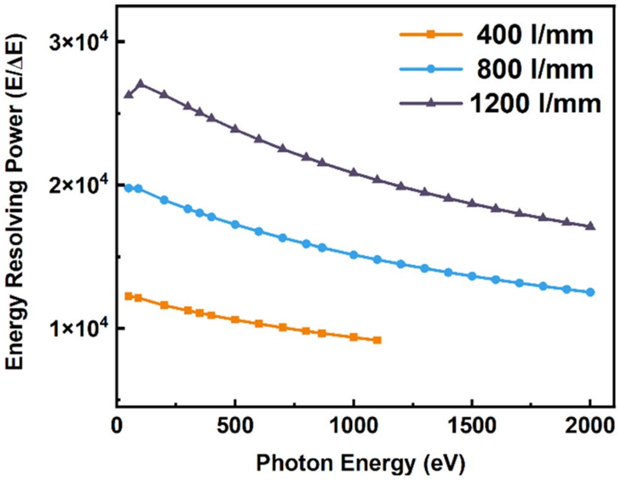

Fig. 2 (Color online) Energy-resolving power of three gratings, which are abbreviated as G400 (orange), G800 (blue), and G1200 (gray), of SSRF BL07U as a function of photon energy ranging from 50 to 2000 eV

3 Experimental method

The BL07U beamline was designed with four end-stations and featured two branches with an angle of 5.6° between them. The operating statuses of these two branches were switched using CM3/PM4 mirrors. The nano-ARPES end-station was constructed at 46.75 m, whereas the other three end-stations, including a spin-ARPES end-station, were constructed at 50 m. A vector magnetic field end-station at 52.9 m and a high magnetic field end-station at 54.9 m shared another branch.

3.1 Nano-ARPES

Third-generation synchrotron light sources are based on the design of synchrotron light with high emission performance. The nano-ARPES end-station prefers to focus on insert installation to achieve better synchrotron light performance. In recent years, spatially resolved ARPES based on synchrotron radiation has emerged as a new direction in the development of ARPES technology. The main idea is to microfocus synchrotron light to submicron/hundred nanometer scales or smaller, in addition to ensuring a high-stability sample design and the relative rotation of the analyzer and sample, to achieve an electronic structure with high spatial resolution for ARPES measurements. The nano-ARPES end-station was constructed on a ball bearing with a diameter of ~ 1.9 m to ensure an additional rotating angle of ± 15° (see Fig. 6). The electron energy analyzer and analysis chamber were shielded with a double μ-metal for magnetic shielding. In addition, a UHV sample preparation chamber and a fast-in load-lock chamber were used to perform sample surface treatment using an argon ion gun and irradiation heating modules, where several storage positions were specified for sample loading. In our system, the energy analyzer comprising an analysis chamber and other vacuum components can rotate simultaneously with the bearing, and a suitable design for these connections is proposed. A rectangular flexible flange was affixed between the synchrotron beamline and facility port to satisfy this requirement.

One of the issues that we considered for the nano-ARPES end-station was the loss of the research domain when manipulating the sample for k-spacing mapping. The conventional DA30 energy analyzer manufactured by Scienta Omicron AB Corporation features a deflector angle of ± 15° at a photo

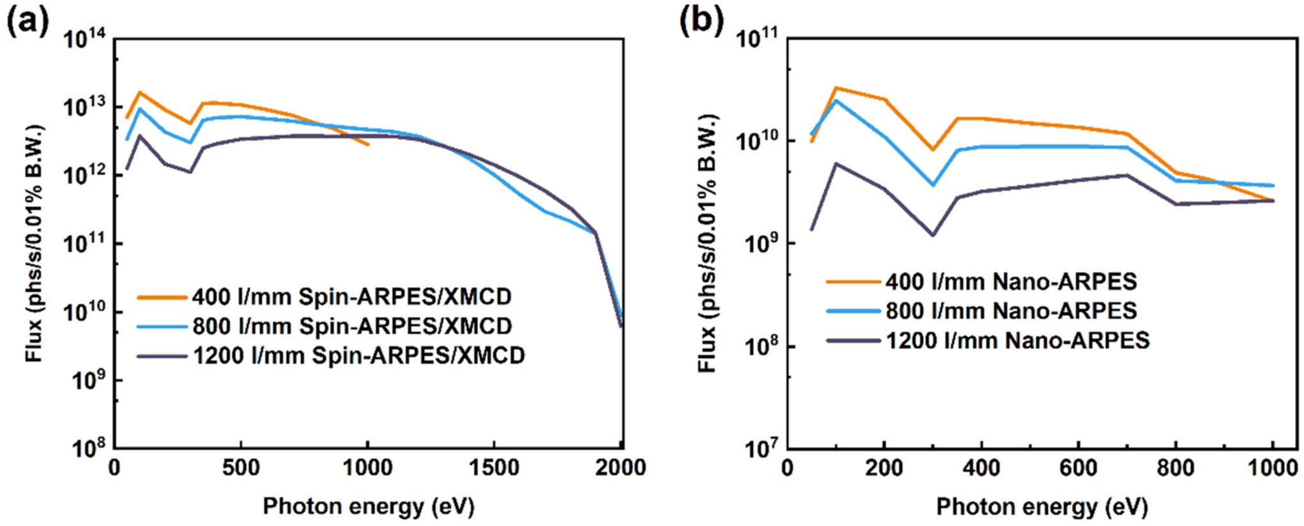

Fig. 3 (Color online) **a** Calculated flux at spin-ARPES/XMCD branch at sample point with circular (Cir) polarization within 50–2000 eV and **b** calculated photon flux after zone plate (ZP) at nano-ARPES branch sample points of G400, G800, and G1200 with circular (Cir) polarization within 50–1000 eV

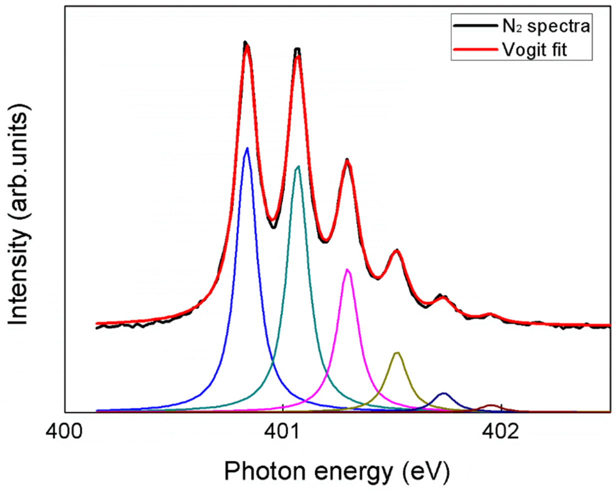

Fig. 4 (Color online) *K*-edge absorption spectrum for N_2 (black) and corresponding fit with superposition of six Voigt lines

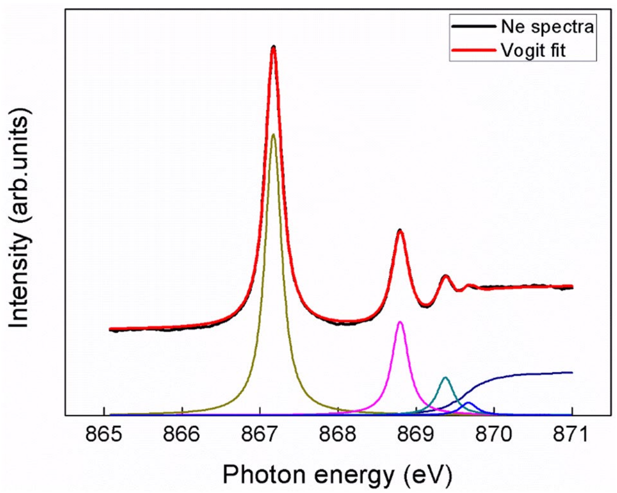

Fig. 5 (Color online) *K*-edge absorption spectrum for Ne (black) and corresponding fit with superposition of six Voigt lines

energy of 100 eV (optional energy usage in our cases), which is insufficient for some samples (such as graphene) with a large Brillouin zone to obtain the band information of the full set. As shown in the nano-ARPES study, a nano/submicron beam size, a sufficiently large scanning area of the sample, and better mechanical repeatability should be considered. Additionally, additional rotation compensation should be considered when designing the system. When rotating the sample for real-time space scanning and measurement, the beam spot cannot return to the same position in exactly the same sample area because of mechanical repeatability. Our nano-ARPES uses a Fresnel OSA to achieve spatially resolved ARPES via spatial diffraction, which affords the smallest spot size (capable of reaching the diffraction limit of X-rays) and easy adjustment. However, the loss of light intensity is significant (1%), and the range of photon energy adjustment is small. To achieve precise spatial scanning, the sample was localized as well as designed with a small spot and high stability. A precision vacuum piezoelectric ceramic displacement stage was used to replace the stepper motor in our ARPES sample holder to achieve a spatial displacement accuracy of 10 nm as well as to position and scan the samples with high precision, as shown in Fig. 7a. However, to improve the positional stability of nano-ARPES

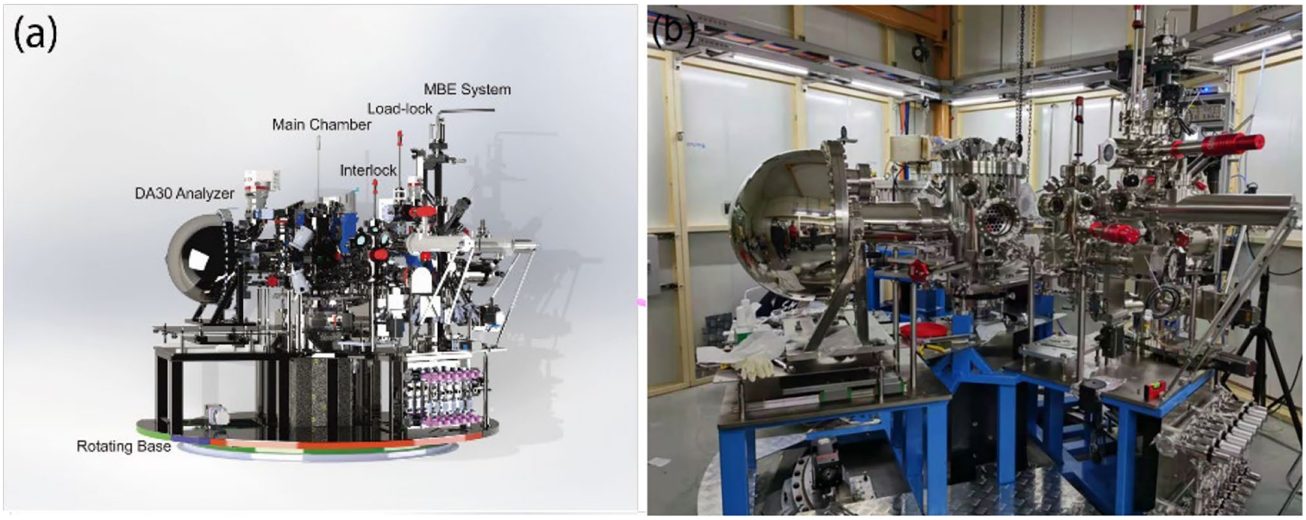

Fig. 6 (Color online) **a** Three-dimensional mechanical drawing of nano-ARPES end-station and **b** photography of the nano-ARPES end-station in SSRF BL07U hatch

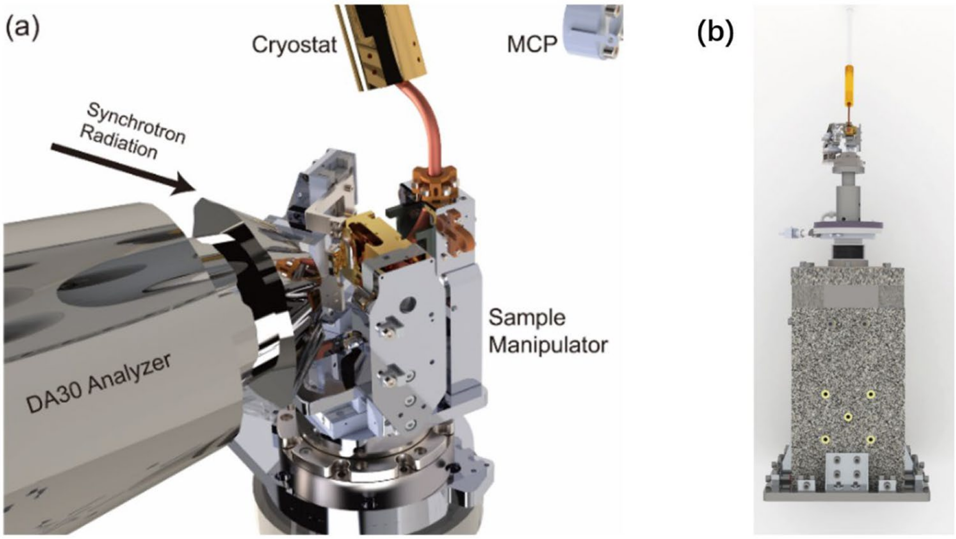

Fig. 7 (Color online) **a** Arrangement inside DA30 analyzer and **b** piezo stage for detector with rotating function

measurement, the sample stage was placed on top of a large mass granite pedestal under a UHV environment, which was used in conjunction with a precision piezoceramic motor to achieve a positional drift of < 1 *μm*/day (see Fig. 7b). In spatially resolved ARPES measurements, relative angular rotation occurs when the analyzer is turned to rotate the sample to shift the spot position. Using an electronic energy analyzer (DA30L, Scienta) with a mode for stereo angular imaging can reduce the rotation variation and moving angle during scanning. The beam spot focus kit comprises central unrotated components against the granite background (see Fig. 7) and features an 11-axis piezo-motorized stage. It features an 11-axis degree of freedom, including three translation-motorized behaviors each for the FZP and OAS, and five degrees of sample movement (x, y, z translation mode, one title mode, and one azimuth rotation within the main axis). A compact UHV compatible piezo-motorized stage design was utilized in our system because the focal distance of the FZP was less than 10 mm, and the operating distance of the analyzer was approximately 30 mm. The kit supporting rod was constricted directly into the granite base for stability. Differentially pumped rotary feedthrough was supplied for UHV survival between the rotatory and stationary components within the nano-ARPES system.

For the nano-ARPES beam spot, two factors affect the beam intensity: (1) Beam spot size. The typical nano-ARPES beam spot size is ~ 200 nm, which is 104 times smaller than the regular ARPES beam spot (~ 20 *μm*). (2) Photon flux.

Nano-ARPES uses a Fresnel zone plate for to focus small beam spots. The focusing principle is based on diffraction, which significantly reduces the photon flux. The efficiency of the photon flux is ~ 1% (which depends on the material of the zone plate), which is 103 times smaller than that of the regular ARPES beam flux. Combining these two factors, the beam intensity is 100 times larger (but still smaller than the laser ARPES intensity), whereas the total photons and photoelectrons are 100 times smaller than those of regular ARPES. The high beam intensity can cause beam damage to the samples, particularly after prolonged measurements, and deteriorate the data quality, whereas a small number of photoelectrons impair the data statistics. However, nano-ARPES is applicable to any sample, unlike the conventional synchrotron-based ARPES. No significant space charge effect or beam damage was observed in our study. A small beam spot allows the measurement of samples that cannot be measured accurately in conventional ARPES end-stations, including exfoliated sample flakes, stacked two-dimensional (2D) material heterostructures, and materials with phase separations.

We measured the beam spot size based on the spatial scanning results with standard patterns (metallic line pairs). However, the spot size was not checked regularly during the measurement of the actual samples. Focusing was adjusted for each sample, and the sharpness of the sample features (*e.g.*, edges of electrical pads, sample dents, or protrusions) determines the focusing and measurement of the beam spot. The beam spot size can be evaluated based on the width of the line scan of a sample feature, as shown in Fig. 8.

Nano-ARPES is important for investigating the electronic structures of a wide range of samples, such as (1) samples with strong lattice three-dimensionality, low resolution, and numerous heterogeneous dissociation planes; (2) samples with multiple dissociation planes or spatial phase separation, such as the $K_xFe_{2-y}Se_2$ system [27]; (3) small-sized samples, such as nanosheets and nanowires [28, 29], which can be obtained *via* mechanical stripping, CVD growth, and other methods; and (4) micro- and nanoelectronic devices, which are prepared using micro-nano processing or micro-nano-electronic devices. Additionally, nano-ARPES can be applied widely to the modulation of electronic structures in a wide range of quantum materials. For example, for the stress modulation of electronic structures, because stress modulation by mechanical stretching/bending is applicable to thin-layer and small-sized samples (large-sized samples have smaller relative deformations) and may present greater spatial inhomogeneity, spatially resolved angle-resolved photoelectron spectroscopy can be used to investigate the modulation of electronic structures by stress more effectively. Additionally, the gate pressure modulation of the electronic structure of materials is typically investigated using micro- and nanodevices composed of small thin-layer samples and gate electrodes; therefore, nano-ARPES is suitable for measuring the electronic structure of small-sized thin-layer samples and its changes under the gate pressure modulation. These special methods of electronic structure modulation further emphasize the unique significance and importance of spatially resolved ARPES.

3.2 Spin-ARPES

Quantum materials are used extensively in condensed-matter physics research. These materials offer various excellent properties, such as charge density waves, superconductivity, topological surface states, spin density waves, *etc.*, which are common properties relevant to the structure of electrons, including energy, momentum, and spin. To examine these properties, the electronic structures must be verified and measured. Spin- and angle-resolved photoelectron

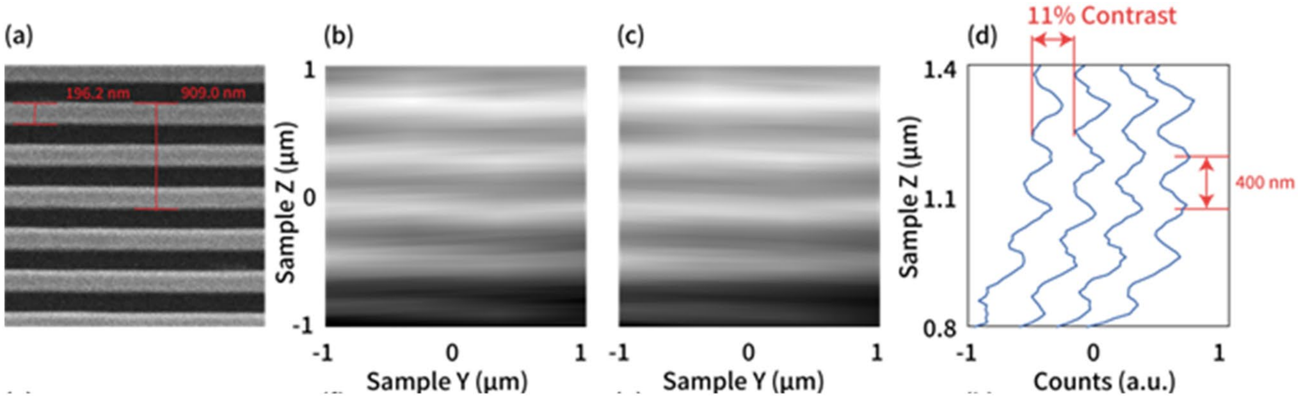

Fig. 8 Standard sample patterns obtained *via* electron beam lithography technique to examine submicron size of focused beam in Nano-ARPES end-station. **a** Scanning electron microscopy (SEM) image of patterns. **b**, **c** Real-space photoemission intensity image of raw image after position correction (without any smooth) acquired from electron analyzer. **d** Plot of raw data of line profiles across golden wire to show more quantitative details

spectroscopy (SARPES), which uses spin-dependent electronic bands in solids, is an effective experimental technique. It can be used to examine the peculiar spin textures of surface states based on the spin–orbit interaction, such as the Rashba spin-splitting state or the helical spin texture of topological insulators [30, 31], as well as to elucidate many-body effects and electron dynamics when investigating complex quantum materials.

In SARPES, a commonly used method is to first allow the electrons to pass through a hemisphere analyzer to detect energy and momentum, and then use spin detectors to detect spin information. However, the efficiency of spin detector-based spin–orbit interactions is on the order of 10^{-4}, which is lower compared with that of regular ARPES. To improve the efficiency of SARPES measurements, researchers developed very low-energy electron diffraction (VLEED) spin detector-based exchange scattering.

To realize three-dimensional spin and angle-resolved photoelectron detectors, the current approach involves installing two Mott-type spin detectors in different directions behind a hemisphere analyzer to achieve three-directional spin detection. Owing to the Mott-type spin detection, the detection efficiency of the detector is low. A better technique is to replace the Mott-type spin detector with a VLEED-type spin detector. However, for the typical VLEED spin detectors, where electrons are incident perpendicular to the iron target, installing a second spin detector to realize spin detection in three-dimensional space is challenging. The BL07U is the first beamline used to construct a spin- and angle-resolved photoelectron detector with electrons incident on an iron target at 45°. Additionally, the detector realizes spin detection in a 2D space.

Figure 9a shows an overview of the experimental system setup, which comprises an analysis chamber, a hemispherical analyzer, a VLEED spin detector, a target preparation chamber, a load-lock chamber, and a molecular beam epitaxy chamber, all of which are vacuum interconnected. The system is equipped with a Xe discharge lamp with a photon energy of 8.43 eV and affords synchrotron radiation with energies ranging from 50 to 2000 eV, thus enabling on- and off-beam measurements.

The analysis chamber is equipped with a custom-designed six degree-of-freedom sample holder with a liquid He cryostat, a hemispherical analyzer, a custom-developed VLEED, and a target preparation chamber. The targets of the VLEED spin detectors are Fe (001)-p (1×1) films terminated with oxygen (Fe(001)-O) grown on MgO (001) substrates, which are in situ prepared in the target preparation chamber [10].

Figure 9b shows a schematic illustration of the spin polarimeter connected to the hemispherical analyzer. The electrons emitted from the sample were separated in energy and momentum directions after passing through the hemispherical analyzer. A 2D image of the band dispersion was obtained at the outlet of the hemispherical analyzer. The electrons from the hemispherical analyzer entered our well-designed spin analyzer. Subsequently, they were reflected by an iron target placed at 45° from the first lens and reached the second lens. Finally, the band dispersion containing energy, momentum, and spin information was gathered by the 2D detector. Additionally, a 2D detector was placed at the end of the first lens. After removing the iron target, we obtained the band dispersion of the spin integration.

In our spin-ARPES system, two sets of electrical lenses were applied to measure the electrical spin information in the *X*- or *Y*-direction by magnetizing the 45° iron target in the *X*- or *Y*-direction. Using an additional third electrical lens and a 2D detector after rotating the Fe target, we

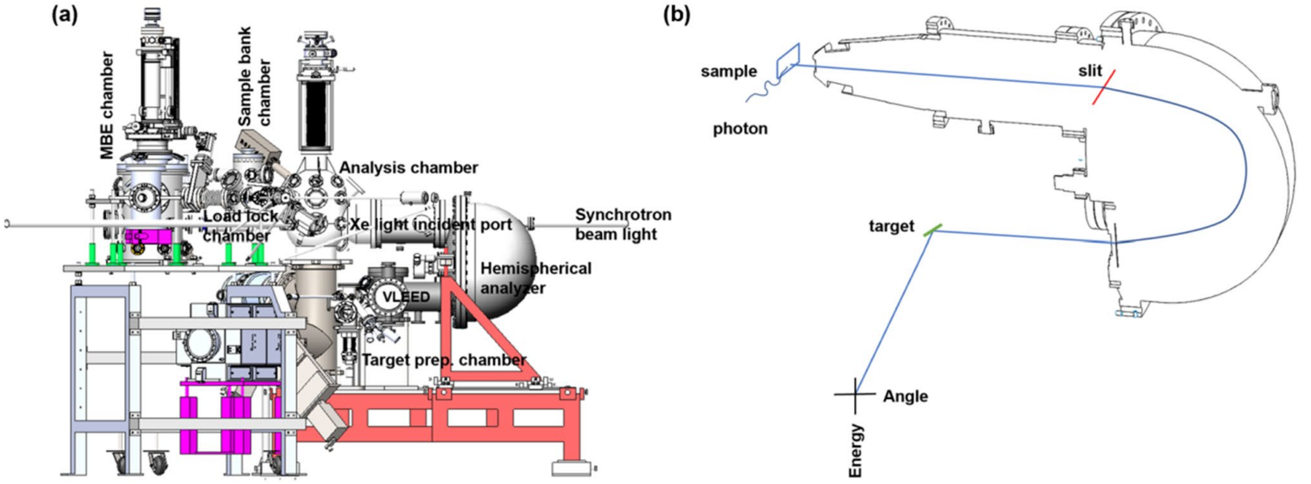

Fig. 9 (Color online) **a** Overview of SARPES equipment and related system of BL07U at Shanghai Synchrotron Radiation Facility. **b** Schematic view of spin polarimeter connected to hemispherical analyzer

successfully achieved magnetization as well as spin information in the *Z*-direction, as shown in Fig. 10. For the measurements, two sets of spin information were obtained by rotating the 45° iron target.

3.3 Vector magnetic end-station

For the XMCD experiments, the BL07U beamline supplied two types of magnetic fields with variable operating temperature ranges for magnetic research.

The first eight-pole electromagnet system utilized and applied in a synchrotron radiation facility in China is shown in Fig. 11. This system is similar to the end-station at Beamline 4.0.2 at the Advanced Light Source [32] and includes six interconnected vacuum pipes, closed-cycle variable-temperature insertion (VTI), four pairs of electromagnetic coils, a yoke iron, a bracket, and a power supply. The six-vacuum channel tubes were utilized for the "in-and-out" X-ray pathways, VTI, load-locking, detection, and observation, separately. The four pairs of electromagnetic coils (or eight electromagnetic coils) were distributed in the eight quadrants of the six vacuum pipes; that is, they were placed diagonally on the cube. Each electromagnetic coil was wound with a copper wire and water-cooled tube, and the lines of magnetic force generated by the four pairs of electromagnetic coils were joined by the yoke iron, which enabled the synthesis of a magnetic field with a maximum value of 0.85 Tesla (main direction of light source) in an any spatial direction of 0.6 Tesla. As shown in Fig. 11, using a sample manipulator that allows a 360° azimuthal rotation of the sample, any geometry of the magnetic field, sample surface, and incident photon direction are permitted. This system can magnetize the sample completely at 15–400 K using a fully helium recondensing insert, which affords a temperature stability of ~ 0.1 K. Additionally, the Mag system features a Hall probe, which allows the magnetic field to be calibrated via online testing.

3.4 Superconductive magnetic end-station

Apart from the vector magnetic end-station, because the magnetic field is insufficient for some antiferromagnetic materials, superconducting magnets are designed and required for higher magnetic fields, which are employed in two split-coil designs, as shown in Fig. 12. Superconducting magnetic fields are typically investigated *via* XMCD and XMLD spectroscopy, which are the same as the vector magnetic end-station method. The main function of this system

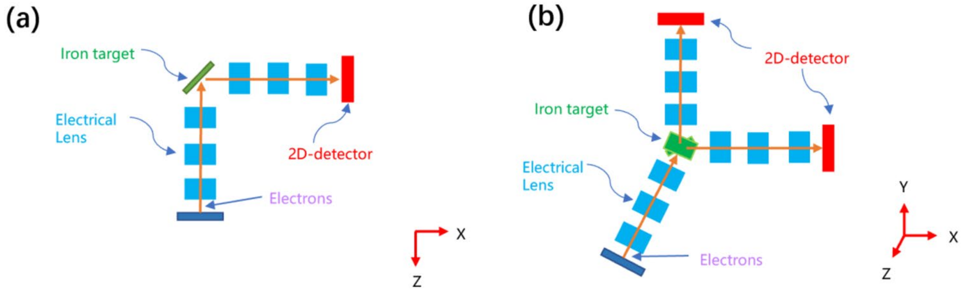

Fig. 10 (Color online) Spin-ARPES end-station of BL07U. **a** Conventional two sets of electric lenses applied currently and **b** upgrade version with additional third electric lens and 2D detector to obtain *Z*-direction by rotating iron target

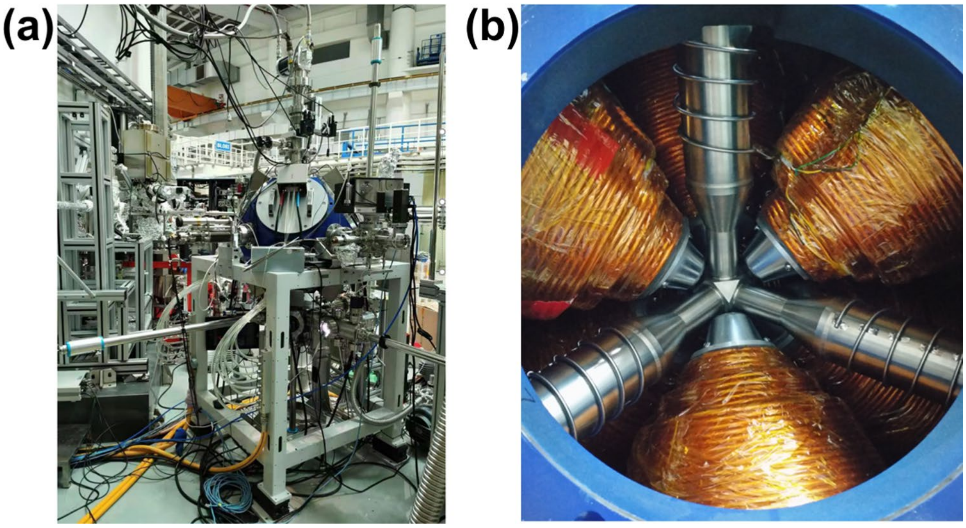

Fig. 11 (Color online) **a** Vector magnetic end-station layout of SSRF BL07U and **b** inside of vector magnets with coils and magnetic yokes

Fig. 12 (Color online) **a** Superconductive magnetic end-station setup of SSRF BL07U; **b** schematic illustration of superconductive magnets within the cryosystem; and **c** six-pin sample adapter for Omicron flag-style sample holder for TEY measurement

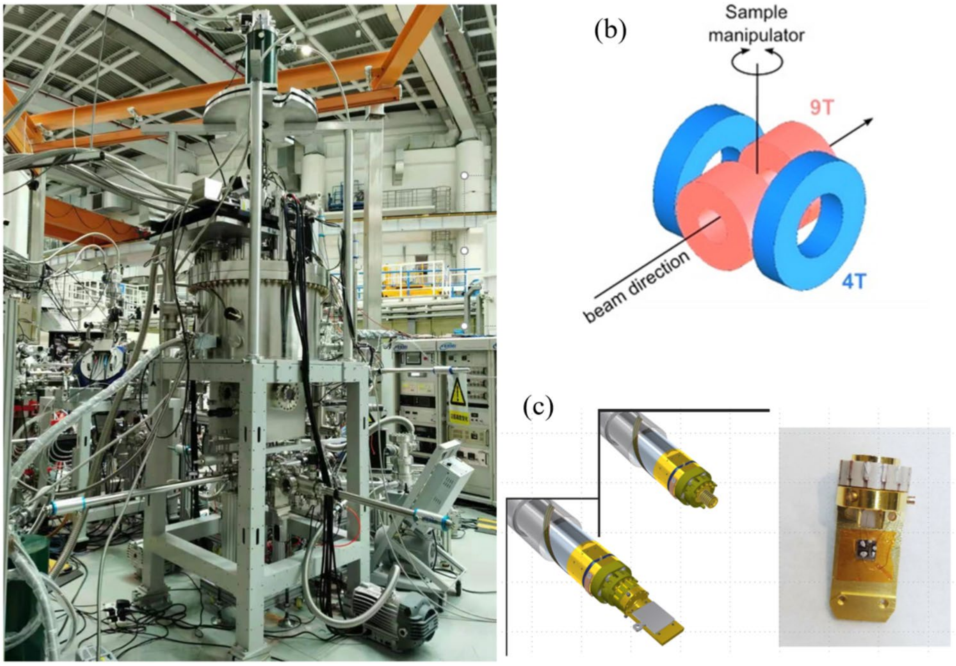

is to provide a sample with a maximum magnetic field of 9 T along the beam direction or 4 T along the horizontal plane perpendicular to the bean direction under ultrahigh-vacuum conditions. Additionally, it allows one to arbitrarily control the sample temperature within the range of 4–350 K and simultaneously measure the total electron yield (TEY) of the sample. Additionally, the VTI system applies a zero-loss liquid helium recycling system, which is the "closed-loop" liquid helium recondensing design used in our system. The superconductive magnets and VTI system were designed and manufactured by Cryogenic Ltd., UK.

The two magnetic field systems used the same sample holder and adaptors, which were fabricated using oxygen-free copper and screwed from the bottom up to the cold finger of the VTI. The cold finger and sample holder comprised six pins, as shown in Fig. 13. Performing interconnection enabled current/electric field excitation to be provided to the sample from outside the vacuum.

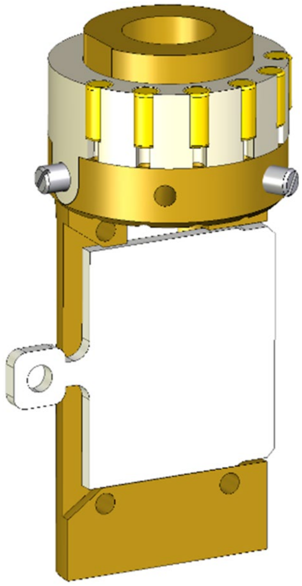

Fig. 13 (Color online) Sample holders for vector magnetic and superconductive magnetic end-stations

3.5 Control and data acquisition system

Figure 14 illustrates the architecture of the control and data acquisition of the BL07U software, which is a distributed architecture. The hardware layer includes all the spectroscopy setups. The control layer controls the spectroscopy setup based on the EPICS. The data acquisition layer performs data acquisition based on the Bluesky suite. These two layers communicate through the Pyepics mechanism. The OPI layer offers a graphical user interface (GUI), which was developed using Control System Studio (CSS). CSS is an OPI application software supported by the EPICS. It offers an OPI layer to communicate with the data acquisition layer through the Pyepics mechanism as well as a control layer through the channel access mechanism [33].

Figure 15 shows the GUI software and the live visualization results. The GUI software comprises a time scan module, normal energy scan module, segmented energy scan module, monochromator, permanent magnet undulator (58/90) linkage scan module, and plot module.

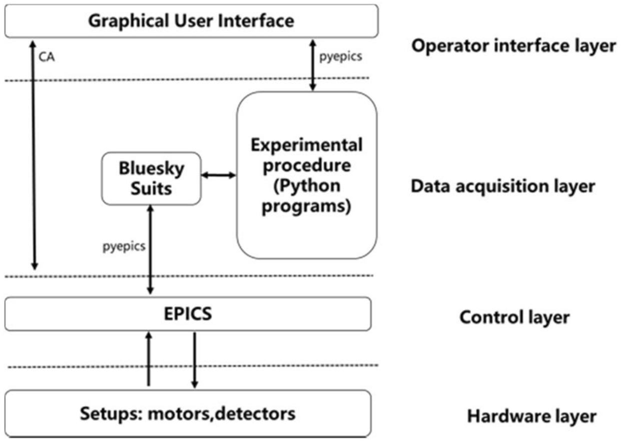

Fig. 14 Control and data acquisition of BL07U software architecture

At the end-stations, the "pump-probe" time-resolved experimental method was developed. Researchers can obtain an electrical signal that synchronizes each photon pulse, and the delay between "pump" and "probe" can be adjusted with a minimum time step of 5 ps [34].

4 First commissioning results

4.1 Nano-ARPES

For the first commissioning results, the moiré superlattice structure of multilayered 2D materials was examined. The structure exhibited abundant unique physical properties and can be adjusted. Bilayer graphene stacked at a specific rotation angle, which is known as the "magic angle," presents important physical properties that are not observed in single-layer graphene, *e.g.*, superconductivity, strong correlation, ferromagnetism, and topology. Recently, Li *et al.* demonstrated that a "magic angle" stacked three-layer graphene not only possessed a superconducting phase diagram similar to that of bilayer graphene but also exhibited a series of novel physical properties, such as a critical magnetic field beyond the Pauli's limit and "re-entrant" superconductivity [35, 36] (see Fig. 16). Using nano-ARPES, the electronic states of the "magic angle" in trilayer graphene were successfully observed. The results revealed the coexistence of Dirac and Mohr energy bands, which is consistent with theoretical predictions (see Fig. 16g). First, the exact position of the "magic angle" three-layer graphene was localized *via* real-space scanning. Subsequently, the coexisting Dirac and Mohr flat bands were observed in momentum space, which is consistent with first-principles calculations. Additionally, the results of scanning tunneling microscopy (STM) provided support to the results of this study, where the Mohr's cycle and the localization of the Mohr flat bands in real space were presented (see Fig. 16e). This corresponds to the extension in momentum space observed *via* nano-ARPES. This study provides the first experimental evidence for the unique energy-band structure of the "magic angle" in trilayer graphene. Furthermore, it demonstrates the significance and potential of the spatially resolved ARPES for investigating low-dimensional materials.

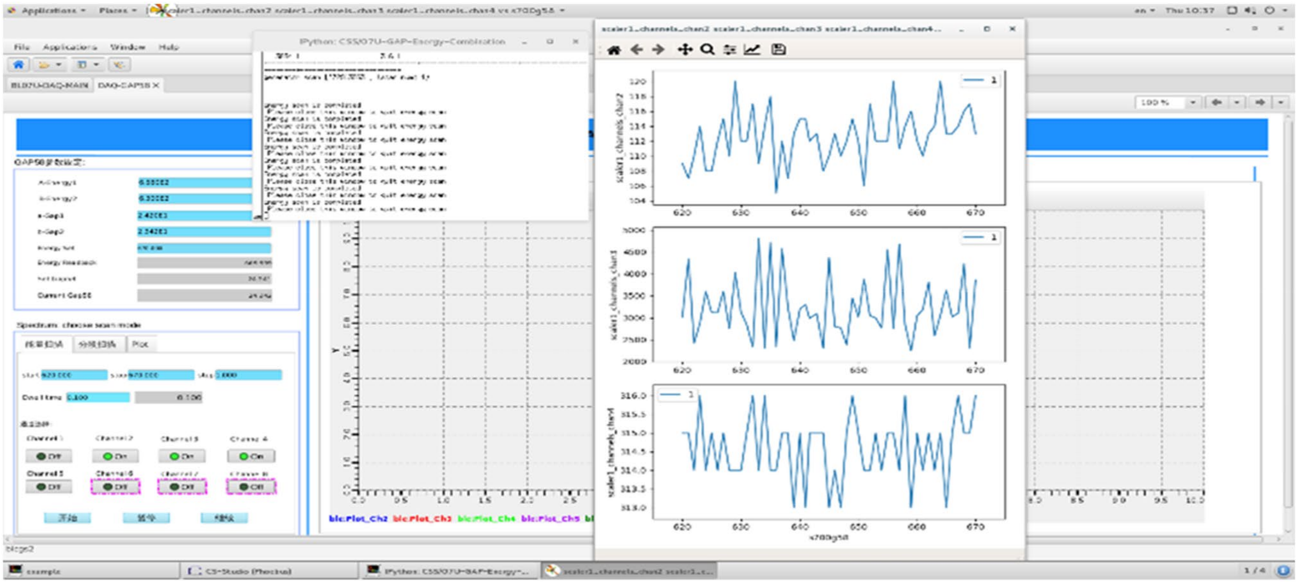

Fig. 15 (Color online) Graphical user interface and live visualization

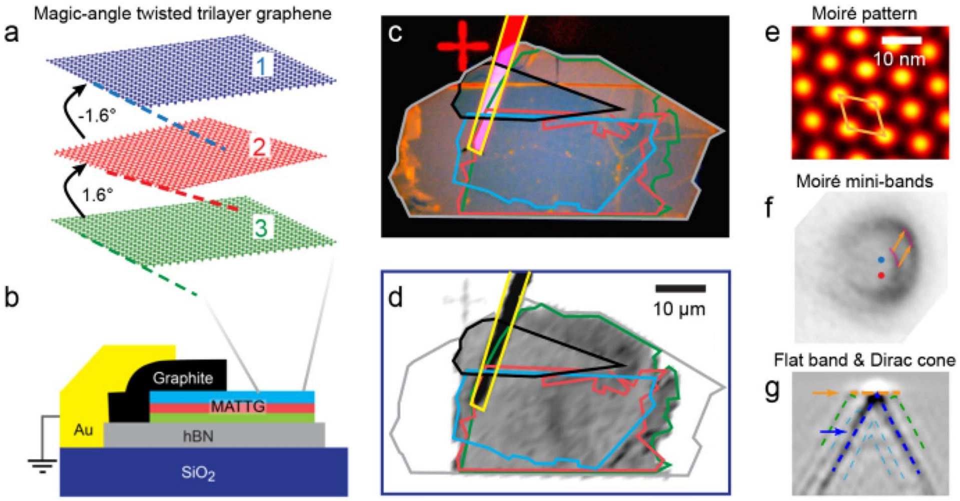

Fig. 16 (Color online) First commissioning results of nano-ARPES based on "magic angle" of three-layer graphene. **a** Schematic illustration of "magic angle" of three-layer graphene stack structure with ± 1.6° for each stack; **b** cross-section illustration of device measurement and operating principle; **c** optical micrograph of device; **d** real-space scanning of device and nano-ARPES measurement; **e** moiré period observed *via* STM; **f** moiré replica band observed *via* nano-ARPES; and **g** coexistence of moiré flat band and Dirac energy band observed *via* nano-ARPES

4.2 Spin-ARPES

To evaluate the performance of the spin-ARPES, we measured a Bi(111) single-crystal thin film grown on a Si(111) surface [37]. Figure 17a shows the Fermi surface mapping of a Bi(111) image at the back of the lens for the spin-integrated ARPES measurement using a Xe discharge lamp (8.43 eV). An electron pocket with a hexagonal shape in the center and six hole pockets were observed, which presented three degrees of symmetry (three light and three dark), likely owing to the threefold symmetry of the bulk Bi crystal and the Bi thin film originating from Rashba splitting [38]. Moreover, we measured the electron-band dispersion along the horizontal lines shown in Fig. 17a. As shown in Fig. 17b, Rashba surface states were clearly detected near the Fermi surface, which is consistent with the mapping of the Fermi surface, and multiple bulk bands were detected. Meanwhile, the band dispersion of Bi (111) under target magnetization was examined. Figure 17c shows the mapping of the Fermi surface obtained under the reflection of the magnetized iron target. Rashba surface states located near the Fermi energy, and the kinetic energy of 3.4–3.6 eV was clearly resolved, as shown in Fig. 17d. To investigate the polarization of the band, we measured the asymmetry of the Rashba surface states by changing the magnetization direction of the iron target, as shown in Fig. 17e–g. Figure 17g shows the spin-resolved Rashba surface-state dispersion, which clearly illustrates the spin splitting of the Rashba surface state. Based on Fig. 17h, which shows the angle distribution curves (ADCs) along the dashed red square region in Fig. 17g, the asymmetry was 0.25. The spin-polarized spectrum of the band under the kinetic energy of 3.4–3.6 eV is shown in Fig. 17i, where asymmetry was clearly observed. The spin-resolved ADCs can be extracted from the 2D spectra with the angle or energy, as shown in Fig. 17k. The asymmetry of the band at the kinetic energy of 3.4–3.6 eV was 0.30. Compared with the reported polarization [39], we obtained an effective Sherman function of 0.42 and a corresponding FOM of 3.2×10^{-2}. Combining this with the number of distinguishable channels, we derived the "two-dimensional figure of merit" [40], $\mathrm{FOM}_{2D} = N \times \mathrm{FOM} = 98.8$, which was approximately 1×10^6 times higher than that of the classic Mott-type single-channel spin polarimeter.

Compared with the conventional single-channel spin detector, the multichannel image spin detector can obtain the spin information of the band efficiently and rapidly in a 2D energy and momentum space with extremely high efficiency. Furthermore, the 45° iron-target reflection-type spin detector can measure the spin information in the third direction after upgrading, thus realizing the measurement of three-dimensional spin, which facilitates investigations into the spin structure of materials, such as topological insulators [41–43], topological semi-metals [44–48], and promotes the development of spin detectors.

4.3 XMCD/XMLD

$SrTiO_3/LaTiO_3/SrTiO_3$ heterostructures with various thicknesses of the $LaTiO_3$ layer (monolayers) were examined to

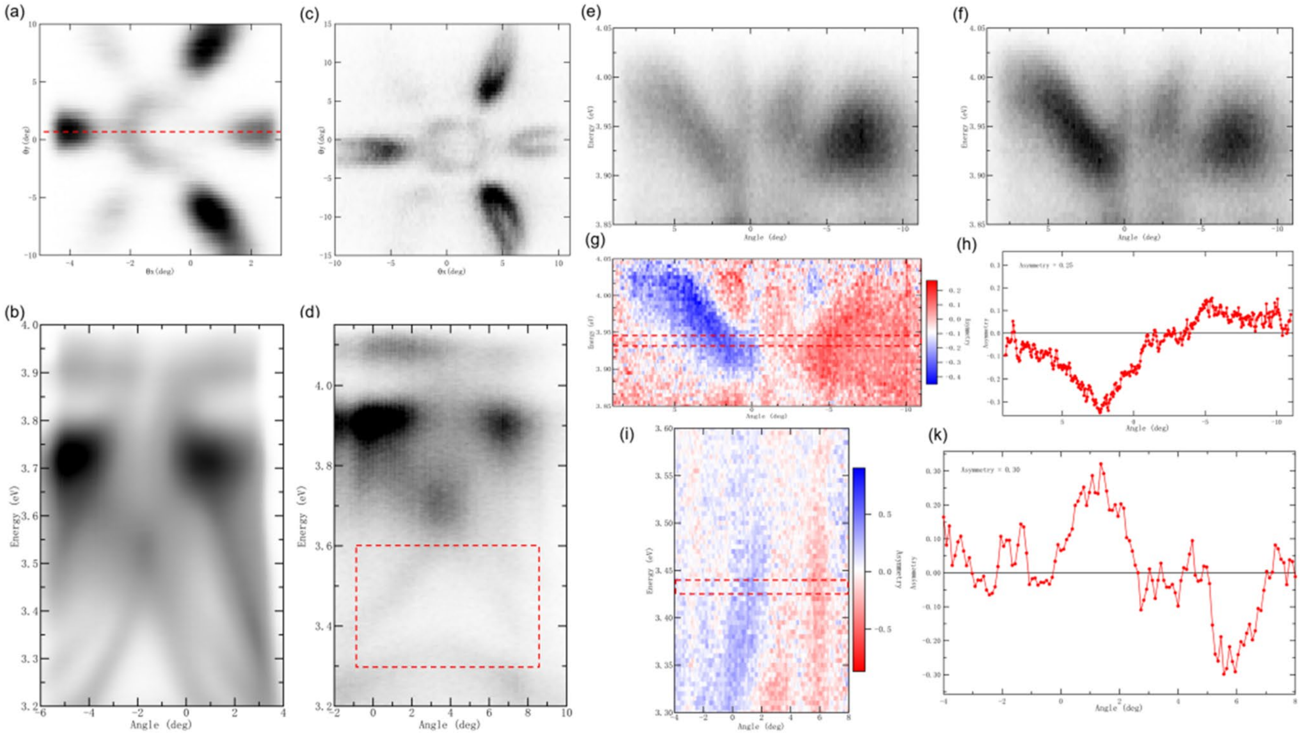

Fig. 17 (Color online) **a** Fermi surface mapping of Bi (111) film obtained using 2D detector of spin-integrated or spin-resolved ARPES mode with Xe discharge lamp. **b** Electron-band dispersions of Bi (111) film along dashed lines in (**a**). **c** and **d** are the same as (**a**) and (**b**) but captured under magnetized iron target. **e**–**g** Spin-resolved spectrum of Rashba state near Fermi surface. **h** Angle distribution curves (ADCs) along dashed red square region of figure (**g**). **f** Spin-resolved spectrum of bulk bands at kinetic energy of 3.4–3.6 eV, corresponding to marked area in (**d**). **k** Angle distribution curves (ADCs) along dashed red square region of figure (**i**)

detect magnetic interactions in the 2D electron gas system. This was performed to understand the principle by which the relationship between localized spin and itinerant electrons at the oxide interfaces was controlled to yield exotic magnetic states, which were reported by Liu *et al.* [49]. The photon energy of the beamline was set at Ti $L_{2,3}$ absorption edges. Polarized X-rays interacted with the sample in the *out-of-plane* ($E//c$) and *in-plane* ($E//ab$) directions, which allowed the absorption spectra to be measured in situ *via* the total electron yield mode at 80 K using the vector magnetic end-station. Simultaneously, the XLD spectra recorded the I_0 (reference beam flux as the background)—I_{sample} value. The TEY was probed at a depth of ~ 5 nm from the surface of the sample. Data counts were obtained from the top-most interface between the $SrTiO_3$ and $LaTiO_3$ layers. The XLD result, as shown in Fig. 18, indicates the splitting of d_{xy} and $d_{xz/yz}$ orbitals at the interface with energy $E_{dxy} < E_{dxz/yz}$, which suggests that both the d_{xy} and $d_{xz/yz}$ bands are located at the Fermi level occupied by carriers and contributed to the electrical transport [49].

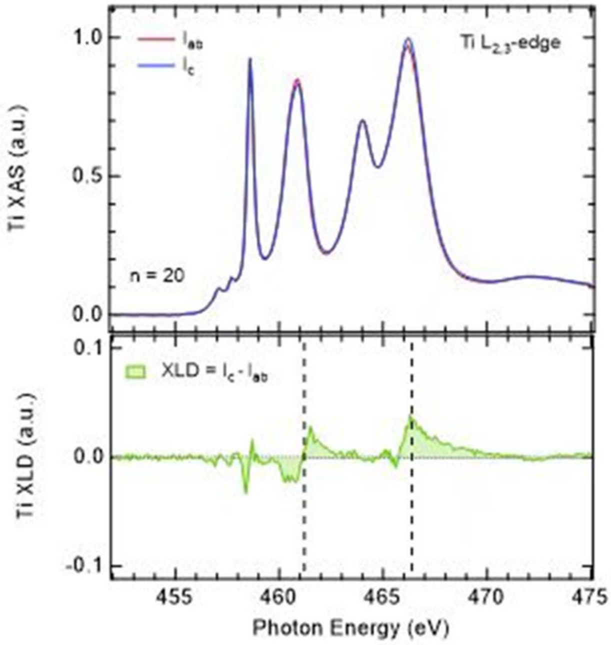

Fig. 18 Soft X-ray absorption spectra (XAS) and X-ray linear dichroism (XLD) spectra of $SrTiO_3/LaTiO_3/SrTiO_3$ with 20 monolayers in $LaTiO_3$. Beamline energy set as Ti L2,3 absorption edge under 80 K for XMLD testing [49]

5 Summary and conclusion

A BL07U beamline with four end-stations was constructed at the SSRF. Because of the use of dual EPUs and the VLS-PGM, the beamlines offered a wide energy range and high energy-resolving power. The four experimental stations exhibited various functions, including spin, spatial, energy, momentum, and time resolutions, which can facilitate investigations into the electronic structure of condensed matter.

Acknowledgements The authors would like to thank all the SSRF supporting staff members, which include the mechanical, front-end and vacuum, control and data acquisition, safety interlock, optical, process, and technical safety groups. In particular, we would like to thank the accelerator group. We appreciate the help extended in operating the SSRF BL07U beamline and in constructing the end-stations.

Author contributions All authors contributed to the study conception and design. Material preparation, data collection, and analysis were performed by Fang-Yuan Zhu, Jie-Feng Cao, Xiang-Yu Meng, Rui Yu, Ya-Mei Wang, Shan Qiao, Bo Zhao, Ming-Zhu Zhang, Zhong-Kai Liu, and Mei-Xiao Wang. The first draft of the manuscript was written by Fang-Yuan Zhu and Jie-Feng Cao. And all authors commented on the previous versions of the manuscript. All authors read and approved the final manuscript.

Data availability The data that support the findings of this study are openly available in Science Data Bank at https://cstr.cn/31253.11.sciencedb.j00186.00126 and https://doi.org/10.57760/sciencedb.j00186.00126.

Declarations

Conflict of interest Ren-Zhong Tai is an editorial board member for Nuclear Science and Techniques and was not involved in the editorial review, or the decision to publish this article. All authors declare that there are no competing interests.

References

1. T. Ito, S. Kimura, H. Im et al., BL5U at UVSOR-II for three-dimensional angle-resolved photoemission spectroscopy. Am. J. Phys. **879**, 587–590 (2007). https://doi.org/10.1063/1.2436129
2. N.A. Artemiev, K.P. Chow, D.J. Merthe et al., Two-foci bendable mirrors for the ALS MAESTRO beamline: design and metrology characterization and optimal tuning of the mirror benders. Adv. X-ray EUV Opt. Comp. VIII SPIE **8848**, 81–95 (2013). https://doi.org/10.1117/12.2024675
3. X. Du, C. Li, S. Wei et al., Construction and performance of combustion beamline at NSRL. AIP Conf. Proc. **1741**, 0300372016 (2016). https://doi.org/10.1063/1.4952860
4. Z.P. Sun, Z.H. Liu, Z.T. Liu et al., Performance of the BL03U beamline at SSRF. J. Synchrotron Rad. **27**, 1388–1394 (2020). https://doi.org/10.1107/s1600577520008310
5. J. Liu, D. Shen, Z. Liu et al., A short introduction to synchrotron radiation-based angle-resolved photoemission spectroscopy end-stations in China. Scientia Sinica Phys. Mech. Astro **53**, 267003 (2023). https://doi.org/10.1360/SSPMA-2023-0031
6. P. Dudin, P. Lacovig, C. Fava et al., Angle-resolved photoemission spectroscopy and imaging with a submicrometre probe at the SPECTROMICROSCOPY-3.2L beamline of elettra. J. Synchrotron Rad. **17**, 445–450 (2010). https://doi.org/10.1107/s0909049510013993
7. J. Avila, A. Boury, B. Caja-Muñoz et al., Optimal focusing system of the Fresnel zone plates at the synchrotron SOLEIL NanoARPES beamline. J. Phys. Conf. Ser. **849**, 012039 (2017). https://doi.org/10.1088/1742-6596/849/1/012039
8. B. Rösner, P. Dudin, J. Bosgra et al., Zone plates for angle-resolved photoelectron spectroscopy providing sub-micrometre resolution in the extreme ultraviolet regime. J. Synchrotron Rad. **26**, 467–472 (2019). https://doi.org/10.1107/s1600577519000869
9. M. Hoesch, T. Greber, V. Petrov et al., Spin-polarized Fermi surface mapping. J. Electron. Spectros. Relat. Phenomena **124**, 263–279 (2002). https://doi.org/10.1016/S0368-2048(02)00058-0
10. T. Okuda, Y. Takeichi, Y. Maeda et al., A new spin-polarized photoemission spectrometer with very high efficiency and energy resolution. Rev. Sci. Instrum. **79**, 123117 (2008). https://doi.org/10.1063/1.3058757
11. Z. Liu, J. Jiang, B. Zhou et al., A stable three-dimensional topological Dirac senimetal Cd3As2. Nat. Mater. **13**, 677–681 (2014). https://doi.org/10.1038/NMAT3990
12. X. Du, L. Kang, Y. Lv et al., Crossed luttinger liquid hidden in a quasi-two-dimensional material. Nat. Phys. **19**, 40–45 (2023). https://doi.org/10.1038/s41567-022-01829-z
13. E. Cheng, W. Xia, X. Shi et al., Magnetism-induced topological transition in EuAs3. Nat. Commun. **12**, 6970 (2021). https://doi.org/10.1038/s41467-021-26482-7
14. Y. Yang, Z. Liu, J. Liu et al., High-resolution ARPES endstation for in situ electronic structure investigations at SSRF. Nucl. Sci. Tech. **32**, 1–13 (2021). https://doi.org/10.1007/s41365-021-00858-2
15. F. Ji, T. Shi, M. Ye et al., Multichannel exchange-scattering spin polarimetry. Phys. Rev. Lett. **116**, 177601 (2016). https://doi.org/10.1103/PhysRevLett.116.177601
16. F. Wilhelm, Magnetic materials probed with polarized X-ray spectroscopies. Synchr. Rad. News **26**, 2–5 (2013). https://doi.org/10.1080/08940886.2013.850370
17. V. Gerrit, I. Adriana, X-ray magnetic circular dichroism—a versatile tool to study magnetism. Coord. Chem. Rev. **277–278**, 95–129 (2014). https://doi.org/10.1016/j.ccr.2014.03.018
18. S. Feng, H. Duan, H. Tan et al., Intrinsic room-temperature ferromagnetism in a two-dimensional semiconducting metalorganic framework. Nat. Commun. **14**, 7063 (2023). https://doi.org/10.1038/s41467-023-42844-9
19. X. Zhang, Q. Lu, W. Liu et al., Room-temperature intrinsic ferromagnetism in epitaxial CrTe2 ultrathin films. Nat. Commun. **12**, 2492 (2021). https://doi.org/10.1038/s41467-021-22777-x
20. L. Xue, R. Reininger, Y. Wu et al., Design of an ultrahigh-energy-resolution and wide-energy-range soft X-ray beamline. J. Synchrotron Rad. **21**, 273–279 (2014). https://doi.org/10.1107/S1600577513029093
21. J. Cao, Y. Wang, Y. Zou et al., Optimization of the design for beamline with fast polarization switching elliptically polarized undulators. J. Synchrotron Rad. **23**, 436–442 (2016). https://doi.org/10.1107/S160057751600059X
22. L. Jin, W.Q. Zhu, Y. Wang et al., A numerical comparison between internal cooling and side cooling of reflection mirror for Spatial and Spin (S2) beam-line at SSRF. Nuclear Inst. Methods Phys. Res. A **902**, 190–196 (2018). https://doi.org/10.1016/j.nima.2018.06.015
23. J. Li, Y. Zou, Z. Chen et al., Ionization chamber based on multi-channel plate and its application on synchrotron radiation. Nuclear Tech. **39**, 050101–050101 (2016). https://doi.org/10.11889/j.0253-3219.2016.hjs.39.050101
24. R.N.S. Sodhi, C.E. Brion, Inner shell electron energy loss spectra of the methyl amines and ammonia. J. Electron Spectrosc.

Relat. Phenom. **34**, 363–372 (1984). https://doi.org/10.1016/0368-2048(85)80017-7

25. A. Barla, J. Nicola's, D. Cocco et al., Design and performance of BOREAS, the beamline for resonant X-ray absorption and scattering experiments at the ALBA synchrotron light source. J. Synchrotron Rad. **23**, 1507–1517 (2016). https://doi.org/10.1107/S1600577516013461
26. U. Gelius, S. Svensson, H. Siegbahn et al., Vibrational and lifetime line broadenings in ESCA. Chem. Phys. Lett. **28**, 1–7 (1974). https://doi.org/10.1016/0009-2614(74)80002-3
27. Y. Chen, J. Jiang, H. Yang et al., Visualization of the electronic phase separation in superconducting KxFe2-ySe2. Nano Res. **14**, 823–828 (2021). https://doi.org/10.1007/s12274-020-3119-8
28. L. Xu, Y. Li, Y. Fang et al., Topology hierarchy of transition metal dichalcogenides built from quantum spin hall layers. Adv. Mater. **35**, 2300227 (2023). https://doi.org/10.1002/adma.202300227
29. C. Liu, Z. Li, R. Qiao et al., Designed growth of large bilayer graphene with arbitrary twist angles. Nat. Mater. **21**, 1263–1268 (2022). https://doi.org/10.1038/s41563-022-01361-8
30. D. Hsieh, Y. Xia, D. Qian et al., A tunable topological insulator in the spin helical Dirac transport regime. Nature **460**, 1101–1105 (2009). https://doi.org/10.1038/nature08234
31. D. Hsieh, D. Qian, L. Wray et al., A topological Dirac insulator in a quantum spin Hall phase. Nature **452**, 970–974 (2008). https://doi.org/10.1038/nature06843
32. E. Arenholz, S.O. Prestemon, Design and performance of an eight-pole resistive magnet for soft x-ray magnetic dichroism measurements. Rev. Sci. Instrum. **76**, 083908 (2005). https://doi.org/10.1063/1.2008027
33. Y. Zhao, C. Hu, C. Wang et al., Data acquisition system based on the Bluesky suite on the shanghai synchrotron radiation facility. Appl. Sci. **13**, 5829 (2023). https://doi.org/10.3390/app13105829
34. X. Yang, J. Cao, J. Li et al., Picosecond time-resolved X-ray ferromagnetic resonance measurements at Shanghai synchrotron radiation facility. Nucl. Sci. Tech. **33**, 63 (2022). https://doi.org/10.1007/s41365-022-01037-7
35. Y. Cao, J. Park, K. Watanabe et al., Pauli-limit violation and reentrant superconductivity in moire graphene. Nature **595**, 526–531 (2021). https://doi.org/10.1038/s41586-021-03685-y
36. J. Park, Y. Cao, K. Watanabe et al., Tunable strongly coupled superconductivity in magic-angle twisted trilayer graphene. Nature **590**, 249–255 (2021). https://doi.org/10.1038/s41586-021-03192-0
37. A. Takayama, T. Sato, S. Souma et al., Giant out-of-plane spin component and the asymmetry of spin polarization in surface Rashba states of bismuth thin film. Phys. Rev. Lett. **106**, 166401 (2011). https://doi.org/10.1103/PhysRevLett.106.166401
38. A. Takayama, T. Sato, S. Souma et al., Rashba effect of bismuth thin film on silicon studied by spin-resolved ARPES. J. Electron. Spectrosc. **201**, 105–109 (2015). https://doi.org/10.1016/j.elspec.2014.11.002
39. T. Okuda, K. Miyamaoto, H. Miyahara et al., Efficient spin resolved spectroscopy observation machine at Hiroshima Synchrotron Radiation Center. Rev. Sci. Instrum. **82**, 103302 (2011). https://doi.org/10.1063/1.3648102
40. M. Kolbe, P. Lushchyk, B. Petereit et al., Highly efficient multichannel spin-polarization detection. Phys. Rev. Lett. **107**, 207601 (2011). https://doi.org/10.1103/PhysRevLett.107.207601
41. C. Chang, K. He, M. Liu et al., Growth of quantum well films of topological insulator Bi2Se3 on insulating substrate. Spin **01**, 21–25 (2012). https://doi.org/10.1142/S2010324711000033
42. O. Yazyev, J. Moore, S. Louie, Spin polarization and transport of surface states in the topological insulators Bi2Se3 and Bi2Te3 from first principles. Phys. Rev. Lett. **105**, 266806 (2010). https://doi.org/10.1103/PhysRevLett.105.266806
43. Y. Chen, J. Analytis, J. Chu et al., Experimental realization of a three-dimensional topological insulator, Bi2Te3. Science **325**, 178–181 (2009). https://doi.org/10.1126/science.1173034
44. M. Hasan, C. Kane, Colloquium: topological insulators. Rev. Mod. Phys. **82**, 3045–3067 (2010). https://doi.org/10.1103/RevModPhys.82.3045
45. H. Qian, X. Zhang, C. Liu et al., Layer-locked spin states revealed in the centrosymmetric nodal-line semimetal HfSiS. Phys. Rev. B **104**, 035145 (2021). https://doi.org/10.1103/PhysRevB.104.035145
46. D. Takane, Z. Wang, S. Souma et al., Dirac-node arc in the topological line-node semimetal HfSiS. Phys. Rev. B **94**, 121108R (2016). https://doi.org/10.1103/PhysRevB.94.121108
47. S. Kobayashi, M. Sato, Topological superconductivity in dirac semimetals. Phys. Rev. Lett. **115**, 187001 (2015). https://doi.org/10.1103/PhysRevLett.115.187001
48. Z. Wang, H. Weng, Q. Wu et al., Three-dimensional Dirac semimetal and quantum transport in Cd3As2. Phys. Rev. B **88**, 125427 (2013). https://doi.org/10.1103/PhysRevB.88.125427
49. F. Yang, Z. Wang, Y. Liu et al., Engineered Kondo screening and nonzero Berry phase in $SrTiO_3/LaTiO_3/SrTiO_3$ heterostructures. Phys. Rev. B **106**, 165421 (2022). https://doi.org/10.1103/PhysRevB.106.165421